CRYSTAL GROWTH & DESIGN

Article

pubs.acs.org/crystal

In Situ Site-Specific Gallium Filling and Nanograin Growth for Blocking of Threading Defects in Semipolar (11$\bar{2}$2) GaN

Zhengyuan Wu,[†,‡] Pengyu Song,[†,‡] Tienmo Shih,[†,§] Linna Pang,[∥] Li Chen,[†] Guangyang Lin,[†] Dingqu Lin,[†] Cheng Li,[†] Ran Liu,[‡] Wenzhong Shen,[∥] Junyong Kang,[†] and Zhilai Fang*[,†,‡]

[†]Collaborative Innovation Center for Optoelectronic Semiconductors and Efficient Devices, Department of Physics, Xiamen University, Xiamen 361005, China

[‡]Engineering Research Center of Advanced Lighting Technology, Ministry of Education, and School of Information Science and Technology, Fudan University, Shanghai 200433, China

[§]CKX Laboratories, Changkeng, 362421, China

[∥]Key Laboratory of Artificial Structures and Quantum Control (Ministry of Education), Department of Physics, Shanghai Jiao Tong University, Shanghai 200240, China

ABSTRACT: Undesirable nonuniformly distributed defects and mixed ($\bar{1}$103) and (11$\bar{2}$2) phases during the growth of semipolar GaN films on m-plane sapphire substrates have been known to exist. In our study, we developed an interface-modification technique to achieve in situ site-specific Ga filling, nucleation, and nanograin growth, which efficiently blocked threading defects there. We have identified the mechanism governing the site-specific Ga filling and nanograin growth into Ga-rich islands based on surface atomic structures and theories of Gibbs free energy. Using the interface modification, we have achieved high-quality semipolar (11$\bar{2}$2) GaN films that enjoy merits of a very low basal-plane stacking fault density of ~9 × 10^3 cm^{-1}, a low threading dislocation density of ~9 × 10^7 cm^{-2}, and the strong band-edge-emission-dominated luminescence.

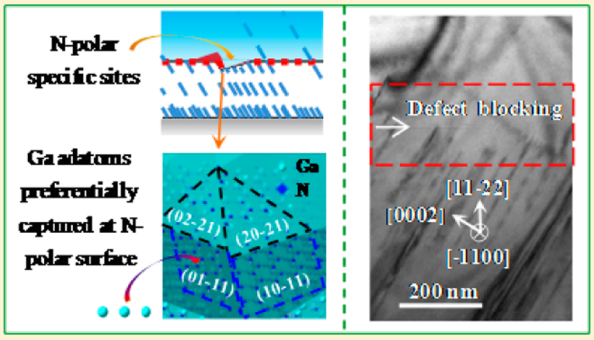

INTRODUCTION

Semipolar (11$\bar{2}$2) group-III nitrides materials have attracted considerable research interests in the field of high-performance optoelectronic devices[1] due to their merits of (a) nearly free electric fields along the growth orientation,[2,3] (b) the wide growth window,[4−6] (c) and the high indium incorporation efficiency.[7,8] Currently, various heterosubstrates have been employed to grow semipolar GaN films[9−13] due to a lack of large-sized and low-priced bulk GaN substrates. However, semipolar (11$\bar{2}$2) GaN heteroepitaxial films are involved with mixed phases, rough surface, and high-density structural defects (dislocation density in the range of 10^{10} cm^{-2} and stacking fault density in the range of 10^5 cm^{-1}).[13,14] Various methods such as SiN_x or ScN or superlattice interlayering,[15−17] two-step growth method,[18,19] epitaxial lateral overgrowth (ELO),[20] patterned sapphire substrates (PSS),[21,22] and in situ asymmetric island sidewall growth[23] have been developed to reduce the density of threading dislocation (TD), partial dislocation (PD), and stacking fault (SF) in semipolar (11$\bar{2}$2) GaN.

For semipolar (11$\bar{2}$2) GaN improved by such methods, undesirable nonuniformly distributed defects[20,21] continue to be located at the mere presence of −c regions (e.g., −c wings in ELO or PSS)[20] and the coalescence boundaries[24,25] that will become arrow-like structures (arrow-shape-morphology coalescence boundaries).[21,26] If the propagation of these defects can be efficiently stopped, qualities of the subsequent layer can be further improved.[27,28]

In the present study, based on surface atomic structures and theories of Gibbs free energy,[29,30] we have developed an interface-modification technique by in situ site-specific growth of Ga-rich islands on these arrow-like structures, which is expected to block the propagation of these defects. The interface-modification technique is different from the SiN_x or ScN interlayering,[15,16] which usually requires ex situ processes and serves as dielectric mask for subsequent ELO of GaN. We have identified the mechanism governing the site-specific Ga filling, Ga-rich island growth, and the Ga-rich surface formation. Using the interface modification, we have achieved high-quality semipolar (11$\bar{2}$2) GaN on sapphire substrates. The interface-modification technique and the further understanding of the mechanism are of general scientific significance as well as of technological application significance in growth of high-quality epitaxial thin films.

Received: April 24, 2017
Revised: July 9, 2017
Published: August 2, 2017

DOI: 10.1021/acs.cgd.7b00584
Cryst. Growth Des. 2017, 17, 4687−4693

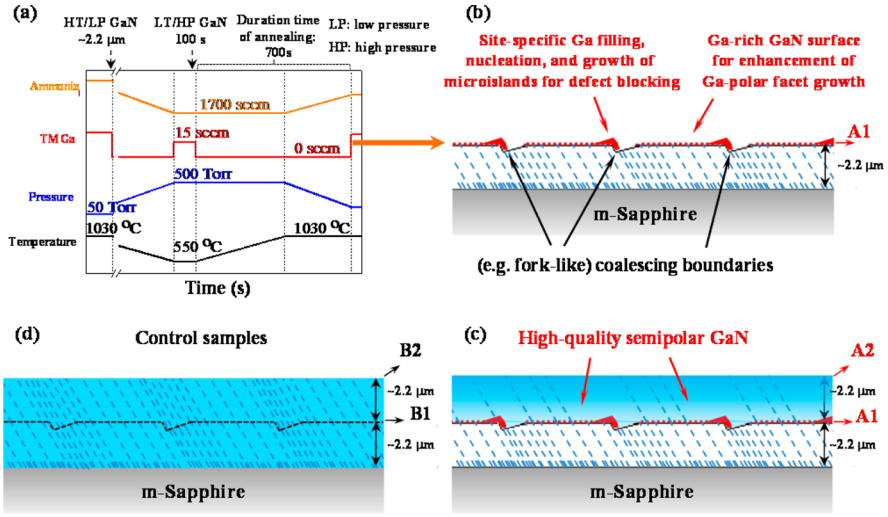

Figure 1. (a) A chart for growth details of GaN microislands and Ga-rich surface. Schematic diagrams of (b) site-specific Ga filling, growth of microislands, and formation of Ga-rich GaN surface on ~2.2 μm HT GaN layer surface (sample A1), (c) a subsequent ~2.2 μm HT GaN layer deposited on sample A1 (sample A2), and (d) HT semipolar (11$\bar{2}$2) GaN layers without interface modification (control samples B1 and B2).

MECHANISM GOVERNING SITE-SPECIFIC GALLIUM FILLING, NANOGRAIN GROWTH, AND GALLIUM-RICH SURFACE FORMATION

We will start describing the crux of the present work, which precisely refers to the procedure conducted in our laboratory. On m-plane sapphire substrates, we conduct the growth of a high-temperature (HT) semipolar (11$\bar{2}$2) GaN layer (sample B1, ~2.2 μm) at 1030 °C under 50 Torr, as traditionally performed.[23] On this layer surface, a GaN layer is deposited under 550 °C and 500 Torr for 100 s, followed by an annealing process for 700 s in H_2 ambience (Figure 1a). During the first 100 s, under high pressure at low temperature, dense nanograins (~7 × 10^8 cm^{-2}) grow on the surface of the semipolar HT GaN layer. The growth of these nanograins is caused by quasi-3D growth mode at high-density-dangling-bond sites (e.g., defects and step edges), resulting from low Gibbs free energy[30] and low Ga-diffusion length under low temperature and high pressure.[31] During the following annealing duration of 700 s, three distinctive growth processes occur: (a) decomposition, (b) in situ site-specific Ga filling, nucleation, and continual growth of nanograins into microislands, and (c) formation of the Ga-rich surface (sample A1, Figure 1b).

In (a), most nanograins decompose into N and Ga, the latter of which can return to serve as the material source for (b) and (c). In (b), Ga filling and nucleation at some specific sites and grow into Ga-rich islands (~1.2 × 10^6 cm^{-2}). These sites are exemplified by triangular cavities (corner-like shape position), steps (stair-like shape position),[30] and structural defects in fork-like ridges (fork-shape-morphology coalescence boundaries, i.e., arrow-like structure) or step-like coalescence boundaries. To nucleate and grow into microislands, nanograins formed by Ga filling and nucleation need to satisfy following three conditions: (i) these specific sites are N-polar, (ii) nanograins must deposit at specific sites (e.g., fork-like ridge) that possess low Gibbs free energy or high-density structural defects,[32] and (iii) nanograin sizes must exceed a critical size, r_c. In (i), the N-polar surface is preferred for adsorption of Ga adatoms (Ga filling), nucleation, and nanograin growth. In (ii), the Gibbs free energy in the half-crystal model can be obtained by the supersaturated chemical potential ($\Delta\mu$): $\Delta\mu = 4 \times \sigma/n$ (per nanometer square), where σ denotes (11$\bar{2}$2) surface energy (per nanometer square) and n denotes the number (per nanometer square) of atoms in different sites. We can deduce n_p (the number of atoms in triangular cavity) > n_b (the number of atoms in step) > n_s (the number of atoms in smooth surface), implying $\Delta\mu_p < \Delta\mu_b < \Delta\mu_s$, and further confirming the existence of the lowest Gibbs free energy in fork-like ridges. In (iii), according to Thomson−Gibbs equation, $dG = dG_v + dG_s = \mu_v dn_v + \mu_c dn_c + \sigma dS$, the r_c value can be obtained by $dG/dr = 0$, i.e., $-12\pi r^2\Delta\mu/(3\Omega) + 8\pi r \times \sigma = 0$, leading to $r_c = 2 \times \sigma \times \Omega/\Delta\mu$, where σ denotes (11$\bar{2}$2) surface energy (per molecular area); Ω the molecular volume of GaN; $\Delta\mu$ the supersaturated chemical potential of phase transition from vapor to crystal (under high pressure and low temperature). The supersaturated chemical potential can be expressed as $KT\ln(P_G/P_0)$, where K denotes the Boltzmann constant; T the growth temperature; P_0 the equilibrium vapor pressure; and P_G the growth vapor pressure. The growth of grains is driven by the presence of the high pressure (P_G) and metallic Ga atoms surrounded by ammonia and hydrogen molecules.

After discussions of the site-selective Ga-rich island growth, let us further clarify the defect-blocking mechanism of these microislands below. Some structural defects, containing misfit dislocation, stacking fault, and tiny void, are usually generated during Ga filling, nucleation, and coarsening of Ga-rich GaN nanograins into microisland. These defect-imbedded microislands can efficiently stop the propagation of defects in the vicinity of fork-like ridges and step-like coalescence boundaries (Figure 1c). In (c), the Ga richness, which originates from the existence of some metallic Ga as surfactants,[33] enhances the Ga-face growth. Subsequently, this enhancement suppresses N-face growth in the subsequent layer of semipolar (11$\bar{2}$2) GaN,[23,34,35] and increases the adatom lateral diffusion (Figure 1b).[31]

The combination of these three growth processes leads to the formation of the Ga-rich surface and Ga-rich microislands site-selectively aggregating on fork-like ridges or other coalescence boundaries. Finally, relying on this formation, we can obtain a high-quality HT semipolar (11$\bar{2}$2) GaN layer with a smooth surface (sample A2, Figure 1c). Simultaneously, for

DOI: 10.1021/acs.cgd.7b00584
Cryst. Growth Des. 2017, 17, 4687−4693

comparison purposes, we prepare HT semipolar (11$\bar{2}$2) GaN layers without this formation (samples B1 and B2, Figure 1d) to confirm impacts of the in situ site-specific Ga filling, Ga-rich microislands, and the Ga-rich surface on crystalline qualities, crystalline phases, and surface smoothness. Samples A2 and B2 were prepared by a subsequent layer growth of ~2.2 μm HT GaN on samples A1 and B1.

CHARACTERIZATION METHODS

All semipolar (11$\bar{2}$2) GaN films on (1$\bar{1}$00) m-plane sapphire substrates were grown in a metalorganic chemical vapor deposition system (Thomas Swan, close-coupled showerhead 3 × 2″ reactor). Trimethylgallium and high-purity ammonia were used as source precursors, and hydrogen as the carrier gas.

Surface stoichiometric information was analyzed by X-ray photoelectron spectroscopy (XPS, PHI Quantum2000) with an Al K_α X-ray excitation source ($h\nu$ = 1486.6 eV). Surface morphologies of semipolar GaN epilayers were investigated by scanning electron microscopy (SEM, Hitachi-SU70) and atomic force microscopy (AFM, SII SPA400). Samples A1 and B1 were etched via the 1 M KOH solutions at 85 °C for 120 s. X-ray diffraction (XRD, PHILIPS X'Pert PRO) and Raman spectroscopy (RAMAN-11) were used to qualitatively analyze the crystalline quality of the semipolar GaN. The luminescence property of the semipolar GaN was investigated by photoluminescence (PL) at 300 K and cathodoluminescence (CL, Model iHR320 Spectrometer System) at 88 K with an electron acceleration voltage of 20 kV and a beam current at 95 nA. The microstructures of samples A2 and B2 were investigated by transmission electron microscopy (TEM, JEM2100) and selected area electron diffraction (SAED) using an accelerating voltage of 200 kV.

RESULTS AND DISCUSSION

Both the existence and critical characteristics of Ga-rich surface are analyzed by XPS spectra (Figure 2) which are referenced to

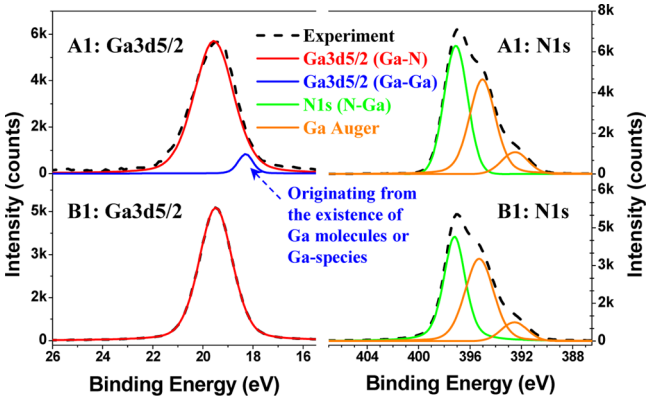

Figure 2. XPS spectra of Ga 3d5/2 photoelectron peak and N 1s photoelectron peak for samples A1 and B1. In the figure, fitted peaks of 18.3, 19.5, and 397.0 eV correspond to Ga 3d5/2 (Ga−Ga), Ga 3d5/2 (Ga−N), and N 1s (N−Ga), respectively.

the XPS data book with the C 1s peak fixed at 284.8 eV.[36] The average gallium to nitrogen ratio, calibrated by sensitivity factors, is defined as $X^{S}_{Ga/N} = (I_{Ga3d5/2}/F_{Ga3d5/2})/(I_{N1s}/F_{N1s})$, where S denotes the name of a sample; I the integrated intensity; and F the sensitivity factor ($F_{Ga3d5/2}$ = 0.438 and F_{N1s} = 0.499). Auger signals originating from gallium are intentionally excluded in integrated intensity of the N 1s photoelectron peak. Results of XPS spectra, $X^{A1}_{Ga/N} \approx 1.04$ and $X^{B1}_{Ga/N} \approx 0.99$ for samples A1 and B1 validate the Ga-richness existence on the surface of sample A1, which is attributed to GaN decomposition and subsequent N desorption. As one of advantages, the N-polar {1$\bar{1}$03} facet growth is ultimately suppressed during the growth of the subsequent HT GaN layer.[23,34,35]

Surface morphologies of samples A1 and B1 (Figure 3) present striations (~0.30 μm^{-1}), which are related to

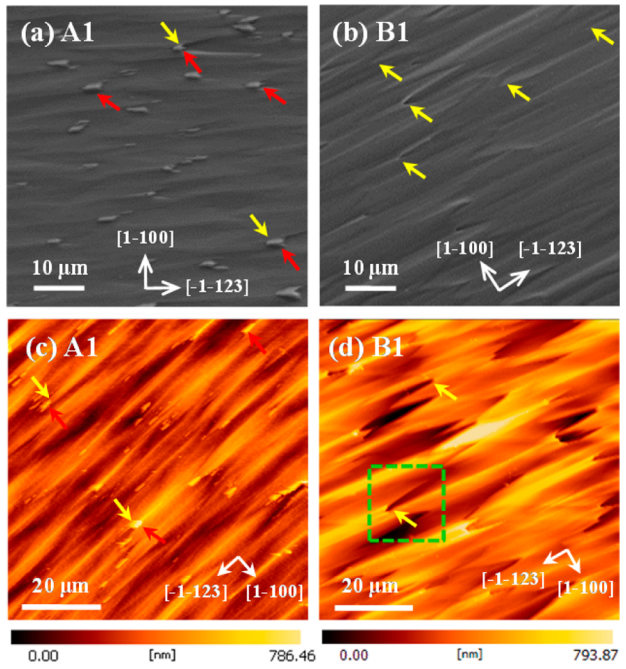

Figure 3. SEM images of samples (a) A1 and (b) B1. AFM images of samples (c) A1 and (d) B1.

anisotropy and defects,[13,17] with typical fork-like ridges (~0.6 × 10^6 cm^{-2}, marked by yellow arrow). Comparing A1 with B1, we observe that microislands (~1.2 × 10^6 cm^{-2}, marked by red arrow) appear in the former, whereas they are absent in the latter. The average lateral size of microislands is roughly estimated as ~3.0 μm along [$\bar{1}$123] and ~1.5 μm along [1$\bar{1}$00] (Figure 3c). The average height of microislands is ~200 nm. The average depth of fork-like ridges is ~250 nm (Figure 3d). These microislands scatter more densely than fork-like ridges do because some of them aggregate on step-like coalescence boundaries.

Figure 4a shows enlarged view of a fork-like ridge, which is green squared in Figure 3d. Figure 4b,c shows line profiles L1 and L2 crossing over sidewall facets of the fork-like ridge. The oblique angles for sidewall facets referring to the (11$\bar{2}$2) plane are ~29° and 25°, indicating the presence of {20$\bar{2}$1} and {10$\bar{1}$1} sidewall facets on the fork-like ridge. Accordingly, a geometrical model for the fork-like ridge is depicted in Figure 4d; the corresponding atomic structure is schematically drawn in Figure 4e. Obviously the fork-like ridges have specific N-polar sidewall facets on the surface. The density of N dangling bonds for the {11$\bar{2}$2}, {10$\bar{1}$1}, and {20$\bar{2}$1} atomic planes is 5.9, 16.2, and 12.1 nm^{-2}, respectively. Therefore, the N-polar {10$\bar{1}$1} and {20$\bar{2}$1} sidewall facets on the fork-like ridge are preferred for adsorption of Ga adatoms. As a result, in situ Ga filling, nucleation, and eventually formation of Ga-rich microislands at these specific sites are achieved, as demonstrated in Figures 2 and 3a,c.

After etching surface morphologies of both samples A1 and B1 (Figure 5) show etched voids (indicated by green arrow) and grooves (yellow arrow) due to the presence of high-density

DOI: 10.1021/acs.cgd.7b00584
Cryst. Growth Des. 2017, 17, 4687−4693

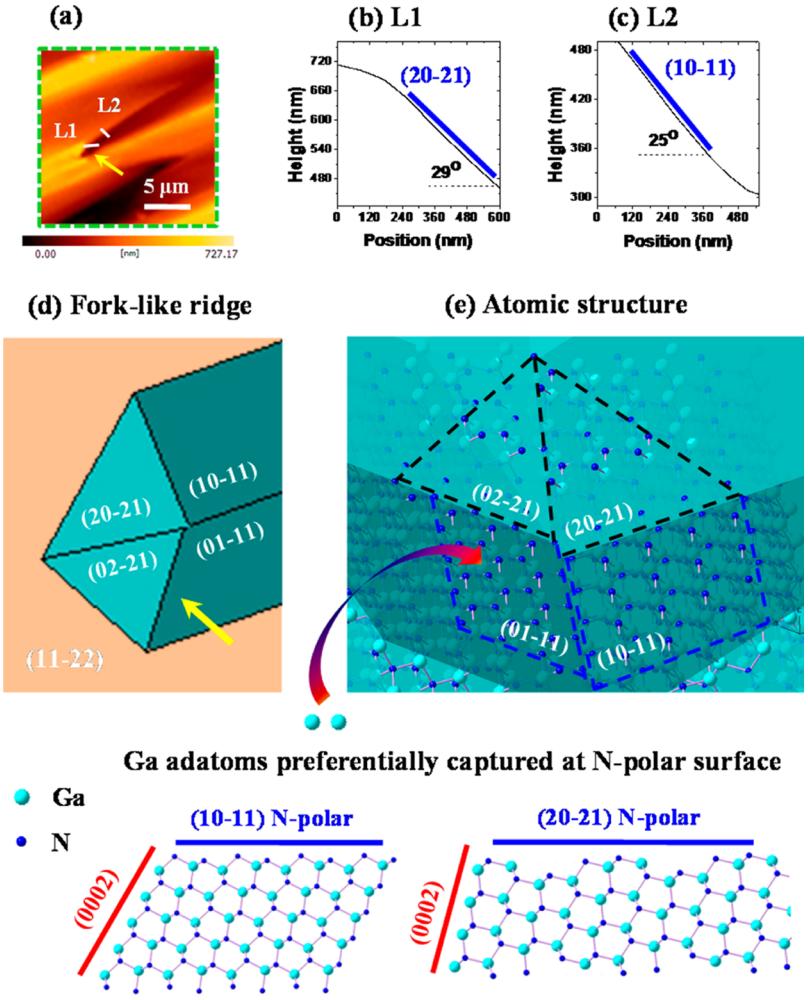

Figure 4. (a) Enlarged view of a fork-like ridge (green squared in Figure 3d). Line profiles crossing over sidewall facets of the fork-like ridge: (b) L1 and (c) L2. (d) Geometrical model showing the fork-like ridge formed on semipolar (11$\bar{2}$2) GaN surface. (e) Schematic diagram of atomic structures for the fork-like ridges with specific N-polar sidewall facets. Cross-sectional view of atomic structures for the (10$\bar{1}$1) and (20$\bar{2}$1) atomic planes is also shown in the figure.

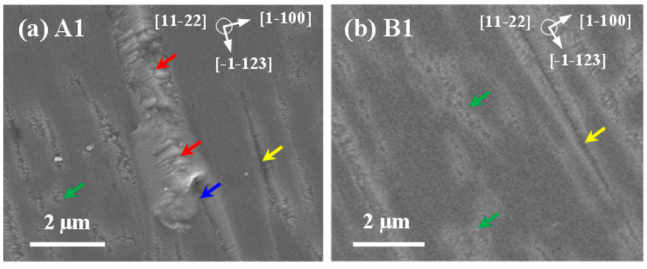

Figure 5. SEM images of samples (a) A1 and (b) B1 after chemical etching with KOH solutions.

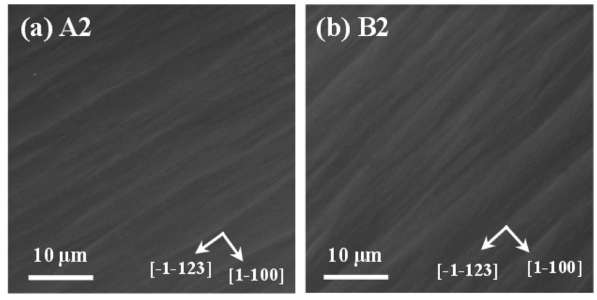

Figure 6. SEM images of samples (a) A2 and (b) B2.

defects and coalescence boundaries there. The microisland (red arrow) on the incompletely covered fork-like ridge (blue arrow) is not etched off; the etched island surface is rough (Figure 5a). This indicates the microisland is defect-imbedded and thus feasible to block threading defects at these sites.

Figure 6 shows surface morphologies of samples A2 and B2. The average striation density of sample A2 is ~0.22 μm^{-1}, which is less than that of A1 (or B2, ~0.30 μm^{-1}), signifying the reduction of defects. Figure 7 shows cross-sectional TEM images of samples A2 and B2 taken along the [$\bar{1}$100] zone axis. Propagation of defects is terminated at the interface between bottom and top HT GaN layers for sample A2 (amber arrows, Figure 7a), which further confirms the defect blocking by interface modification. During the subsequent growth of GaN on microislands, some threading dislocations are bent by image forces and finally annihilated by formation of the dipole half loop (green arrow). No defect blocking effect was observed for sample B2 (Figure 7b). SAED patterns (insets) further support the improvement in crystalline quality of sample A2 compared with that of sample B2.

Crystalline phases in semipolar GaN grown on m-sapphire need to be confirmed by XRD ω-2θ scans due to the existence

DOI: 10.1021/acs.cgd.7b00584
Cryst. Growth Des. 2017, 17, 4687−4693

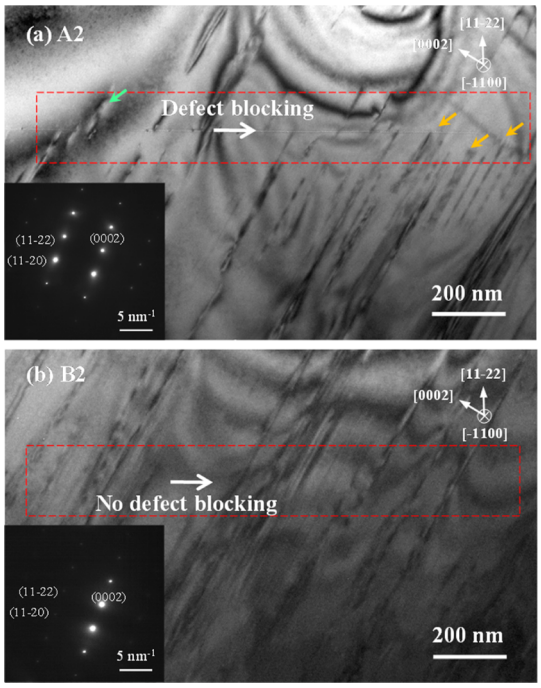

Figure 7. Cross-sectional TEM images of samples (a) A2 and (b) B2. The insets are selected-area-electron-diffraction patterns of samples A2 and B2. White arrows indicate the interfaces between bottom and top HT GaN layers.

of the $(10\bar{1}3)$ phase, which results from the nitridation process or the initial GaN growth[14,23] and thereby lowers the crystalline quality and device performance. Sample A2 shows a single $(11\bar{2}2)$ peak, whereas a $(11\bar{2}2)$ peak at 34.6° and a $(10\bar{1}3)$ peak at 32.2° simultaneously appear in sample B2 (Figure 8a), confirming that the $(10\bar{1}3)$ facet growth has been suppressed by the Ga-rich surface, as mentioned in the description related to XPS spectra. In Figure 8b the XRD ω-scan peak fwhm of sample A2 (100 arcsec) can be observed to be narrower than that of sample B2 (190 arcsec), indicating that the crystalline quality of A2 has been improved via the mechanism aforementioned. This improvement is further demonstrated by data of (a) A2: the basal SF (BSF) density ~9.0×10^3 cm^{-1} and the TD density ~9.0×10^7 cm^{-2}, and (b) B2: the BSF density ~2.2×10^4 cm^{-1} and the TD density ~1.6×10^8 cm^{-2}. These data are obtained via empirically derived fwhm-defect density relationships.[13,16,23] Figure 8c shows fwhm's of $(n0\bar{n}0)$ X-ray rocking curves with the incident beam aligned to the c-axis. The fwhm's of $(10\bar{1}0)$, $(20\bar{2}0)$, and $(30\bar{3}0)$ diffraction peaks from sample B2 are 0.72, 0.52, and 0.34 degree, respectively. The fwhm's of $(10\bar{1}0)$, $(20\bar{2}0)$, and $(30\bar{3}0)$ diffraction peaks from sample A2 are 0.42, 0.30, and 0.25 deg, respectively, which are much smaller than those of sample B2. These further indicate a decrease in BSF density for sample A2 with interface modification.

The Raman E_2^H peak of sample A2 (568.0 cm^{-1}) shifts more closely to the compressive-strain-free position (567.6 cm^{-1})[37] than that of sample B2 (568.3 cm^{-1}) does (Figure 9), with the resolution enlarged (inset). The residual compressive strain σ in samples A2 and B2 can be estimated to be approximately 0.10 and 0.17 GPa from $\sigma = \Delta\omega/K$, where $\Delta\omega$ denotes the peak shift (A2:0.4 cm^{-1}; B2:0.7 cm^{-1}) and K denotes the linear strain coefficient (~4.2 cm^{-1}/GPa). In addition, the fwhm of E_2^H peak (inset) of A2 (5.6 cm^{-1}) appears narrower than that of B2 (6.2 cm^{-1}) does, suggesting that fewer defects are embedded in A2 than in B2.[23] These Raman results do appear consistent with XRD counterparts in terms of fwhm and defect reduction.

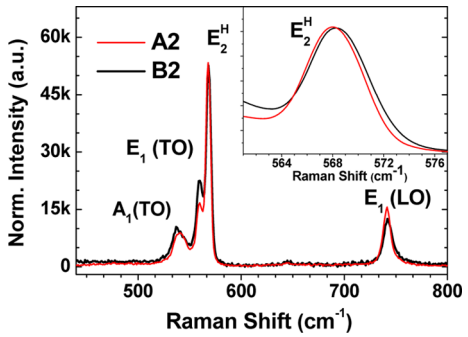

Figure 9. Micro-Raman spectra of samples A2 and B2 with clearly visible E_2^H, E_1(TO), A_1(TO), and E_1(LO) phonon peaks.

Because of the existence of high-density structural defects, semipolar GaN on sapphire generally luminesces weakly, and this luminescence is dominated by the defects-correlated emission.[38,39] The A2 sample, which exhibits high crystalline qualities, luminesces intensively with the band-edge (BE) related peak at 3.40 eV, whereas B2, which contains numerous BSFs, PDs, and prismatic SFs, luminesces weakly with the defects-induced peak at 3.37 eV (Figure 10a). In 88 K CL spectra (Figure 10b), the D^0X emission from sample A2 is enhanced, whereas the SF emission is suppressed compared with that from sample B2; the intensity ratio between D^0X and SF emissions is 1.6 for sample B2 and 5.8 for sample A2, indicating significant reduction of defect density in sample A2.

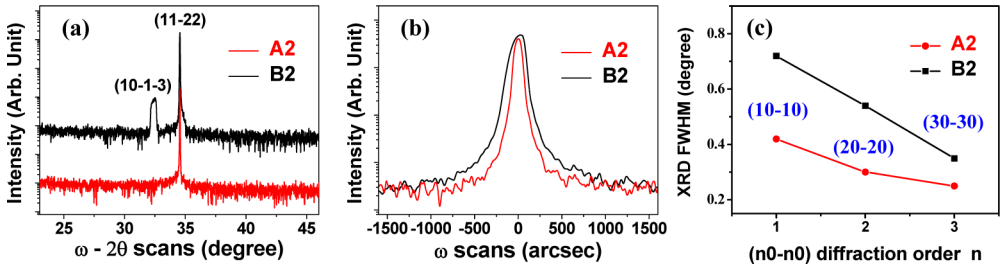

Figure 8. (a) XRD ω-2θ scans of samples A2 and B2. (b) XRD ω scans of $(11\bar{2}2)$ peaks from samples A2 and B2 with the incident beam direction aligned to $[\bar{1}123]$. (c) fwhm's of $(n0\bar{n}0)$ X-ray rocking curves (n = 1, 2, 3) with the incident beam aligned to the c-axis.

DOI: 10.1021/acs.cgd.7b00584
Cryst. Growth Des. 2017, 17, 4687−4693

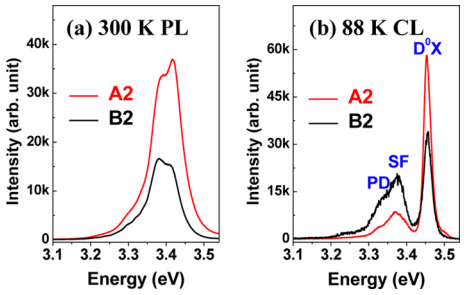

Figure 10. (a) 300 K PL spectra of samples A2 and B2. (b) 88 K CL spectra with emission peak energies of D^0X, SF, and PD at 3.458, 3.375, and 3.328 eV, respectively. The probe area is on the order of 100 × 100 μm^2.

CONCLUSION

We have improved the crystalline quality of semipolar $(11\bar{2}2)$ GaN films on m-plane sapphire substrates using interface modification via site-specific Ga-rich microislands and Ga-rich GaN surface. Furthermore, we have identified mechanisms governing (a) site-specific Ga filling, nucleation, and growth of Ga-rich microislands on fork-like ridges of N-polar sidewall facet surface and (b) defect blocking at these specific sites. These microislands can aggregate on fork-like ridges as well as other coalescence boundaries to efficiently stop the propagation of threading defects located at these boundaries, and this Ga-rich surface enhances the Ga-face growth to achieve pure semipolar $(11\bar{2}2)$ GaN films. The existences of Ga-rich surface and defect-embedded microislands are proven by XPS and KOH etching. With interface modification by in situ site-specific Ga filling and growth of Ga-rich microislands defect blocking effect is evident at the interface as demonstrated by TEM. Via XRD and Raman measurements, a very low BSF density of ~9 × 10^3 cm^{-1} and a low TD density of ~9 × 10^7 cm^{-2} are depicted. Because of the crystalline-quality improvement, the PL is significantly enhanced and dominated by BE emission. In 88 K CL, the D^0X emission is enhanced, whereas the SF emission is suppressed, indicating significant reduction of defect density. The proposed concept may be applied to the growth of various inorganic materials, but not necessarily GaN, and to the design of various structures grown on specific templates.

AUTHOR INFORMATION

Corresponding Author

*E-mail: zhilaifang@hotmail.com.

ORCID

Guangyang Lin: 0000-0003-1784-5029

Zhilai Fang: 0000-0002-9270-5475

Notes

The authors declare no competing financial interest.

ACKNOWLEDGMENTS

This work was supported by the National Natural Science Foundation of China under Grant Nos. 11544008 and 61076091.

REFERENCES

(1) Funato, M.; Kawakami, K. *MRS Bull.* **2009**, *34*, 334−340.
(2) Romanov, A. E.; Baker, T. J.; Nakamura, S.; Speck, J. S. *J. Appl. Phys.* **2006**, *100*, 023522.
(3) Northrup, J. E. *Appl. Phys. Lett.* **2009**, *95*, 133107.
(4) Li, H.; Geelhaar, L.; Riechert, H.; Draxl, C. *Phys. Rev. Lett.* **2015**, *115*, 085503.
(5) Nishizuka, K.; Funato, M.; Kawakami, Y.; Fujita, S.; Narukawa, Y.; Mukai, T. *Appl. Phys. Lett.* **2004**, *85*, 3122−3124.
(6) Imer, B.; Wu, F.; Speck, J. S.; DenBaars, S. P. *J. Cryst. Growth* **2007**, *306*, 330−338.
(7) Zhao, Y.; Yan, Q.; Huang, C. Y.; Huang, S. C.; Hsu, P. S.; Tanaka, S.; Pan, C. C.; Kawaguchi, Y.; Fujito, K.; Van de Walle, C.; Speck, J. S.; DenBaars, S. P.; Nakamura, S.; Feezell, D. *Appl. Phys. Lett.* **2012**, *100*, 201108.
(8) Strittmatter, A.; Northrup, J. E.; Johnson, N. M.; Kisin, M. V.; Spiberg, P.; El-Ghoroury, H.; Usikov, A.; Syrkin, A. *Phys. Status Solidi B* **2011**, *248*, 561−573.
(9) Shetty, S.; Kesaria, M.; Ghatak, J.; Shivaprasad, S. M. *Cryst. Growth Des.* **2013**, *13*, 2407−2412.
(10) Kobayashi, A.; Ueno, K.; Ohta, J.; Fujioka, H. *Phys. Status Solidi A* **2011**, *208*, 834−837.
(11) Chen, H.; Ko, T.; Ling, S.; Lu, T.; Kuo, H.; Wang, S.; Wu, Y.; Chang, L. *Appl. Phys. Lett.* **2007**, *91*, 021914.
(12) Baker, T. J.; Haskell, B. A.; Wu, F.; Fini, P. T.; Speck, J. S.; Nakamura, S. *Jpn. J. Appl. Phys.* **2005**, *44*, L920−L922.
(13) Baker, T. J.; Haskell, B. A.; Wu, F.; Speck, J. S.; Nakamura, S. *Jpn. J. Appl. Phys.* **2006**, *45*, L154−L157.
(14) Ploch, S.; Frentrup, M.; Wernicke, T.; Pristovsek, M.; Weyers, M.; Kneissl, M. *J. Cryst. Growth* **2010**, *312*, 2171−2174.
(15) Jeong, J.; Jang, J.; Hwang, J.; Jung, C.; Kim, J.; Lee, K.; Lim, H.; Nam, O. *J. Cryst. Growth* **2013**, *370*, 114−119.
(16) Moram, M. A.; Johnston, C. F.; Kappers, M. J.; Humphreys, C. J. *J. Cryst. Growth* **2009**, *311*, 3239−3242.
(17) Xu, S. R.; Zhang, J. C.; Cao, Y. R.; Zhou, X. W.; Xue, J. S.; Lin, Z. Y.; Ma, J. C.; Bao, F.; Hao, Y. *Thin Solid Films* **2012**, *520*, 1909−1912.
(18) Kappers, M. J.; Hollander, J. L.; McAleese, C.; Johnston, C. F.; Broom, R. F.; Barnard, J. S.; Vickers, M. E.; Humphreys, C. J. *J. Cryst. Growth* **2007**, *300*, 155−159.
(19) Sun, Q.; Leung, B.; Yerino, C. D.; Zhang, Y.; Han, J. *Appl. Phys. Lett.* **2009**, *95*, 231904.
(20) Vennegues, P. *Semicond. Sci. Technol.* **2012**, *27*, 024004.
(21) Brunner, F.; Edokam, F.; Zeimer, U.; John, W.; Prasai, D.; Kruger, O.; Weyers, M. *Phys. Status Solidi B* **2015**, *252*, 1189−1194.
(22) Tendille, F.; De Mierry, P.; Vennegues, P.; Chenot, S.; Teisseire, M. *J. Cryst. Growth* **2014**, *404*, 177−183.
(23) Wu, Z. Y.; Shen, X. Y.; Liu, C.; Li, K. Y.; Shen, W. Z.; Kang, J. Y.; Fang, Z. L. *CrystEngComm* **2016**, *18*, 5440−5447.
(24) Bottcher, T.; Einfeldt, S.; Figge, S.; Chierchia, R.; Heinke, H.; Hommel, D.; Speck, J. S. *Appl. Phys. Lett.* **2001**, *78*, 1976−1978.
(25) Lotsari, A.; Das, A.; Kehagias, T.; Kotsar, Y.; Monroy, E.; Karakostas, T.; Gladkov, P.; Komninou, P.; Dimitrakopulos, G. P. *J. Cryst. Growth* **2012**, *339*, 1−7.
(26) Zhu, T. T.; Johnston, C. F.; Kappers, M. J.; Oliver, R. A. *J. Appl. Phys.* **2010**, *108*, 083521.
(27) Iwaya, M.; Takeuchi, T.; Yamaguchi, S.; Wetzel, C.; Amano, H.; Akasaki, I. *Jpn. J. Appl. Phys.* **1998**, *37*, L316−L318.
(28) Jung, C.; Jang, J.; Hwang, J.; Jeong, J.; Kim, J.; Lee, K.; Nam, O. *J. Cryst. Growth* **2013**, *370*, 26−29.
(29) Heller, E. J.; Zhang, Z. Y.; Lagally, M. G. *Phys. Rev. Lett.* **1993**, *71*, 743−746.
(30) Markov, I. V. *Crystal Growth for Beginners: Fundamentals of Nucleation, Crystal Growth and Epitaxy*; World Scientific: Singapore, 1995.
(31) Morishita, Y.; Nomura, Y.; Goto, S.; Katayama, Y. *Appl. Phys. Lett.* **1995**, *67*, 2500.
(32) Laboutin, O. A.; Welser, R. E. *Appl. Phys. Lett.* **2008**, *92*, 223103.
(33) Fang, Z. L.; Kang, J. Y.; Shen, W. Z. *Nanotechnology* **2009**, *20*, 045401.
(34) Keller, S.; Li, H. R.; Laurent, M.; Hu, Y. L.; Pfaff, N.; Lu, J.; Brown, D. F.; Fichtenbaum, N. A.; Speck, J. S.; DenBaars, S. P.; Mishra, U. K. *Semicond. Sci. Technol.* **2014**, *29*, 113001.

DOI: 10.1021/acs.cgd.7b00584
Cryst. Growth Des. 2017, 17, 4687−4693

(35) Hiramatsu, K.; Nishiyama, K.; Motogaito, A.; Miyake, H.; Iyechika, Y.; Maeda, T. *Phys. Status Solidi A* **1999**, *176*, 535−543.
(36) Moulder, J. F.; Stickle, W. F.; Sobol, P. E.; Bomben, K. D. *Handbook of X-ray Photoelectron Spectroscopy: A Reference Book of Standard Spectra for Identification and Interpretation of XPS Data*; Physical Electronics: MN, 1995.
(37) Davydov, V. Y.; Kitaev, Y. E.; Goncharuk, I. N.; Smirnov, A. N.; Graul, J.; Semchinova, O.; Uffmann, D.; Smirnov, M. B.; Mirgorodsky, A. P.; Evarestov, R. A. *Phys. Rev. B: Condens. Matter Mater. Phys.* **1998**, *58*, 12899−12906.
(38) Liu, R.; Bell, A.; Ponce, F. A.; Chen, C. Q.; Yang, J. W.; Khan, M. A. *Appl. Phys. Lett.* **2005**, *86*, 021908.
(39) Schwaiger, S.; Argut, I.; Wunderer, T.; Rosch, R.; Lipski, F.; Biskupek, J.; Kaiser, U.; Scholz, F. *Appl. Phys. Lett.* **2010**, *96*, 231905.

DOI: 10.1021/acs.cgd.7b00584
Cryst. Growth Des. 2017, 17, 4687−4693